

# Designing XY and Dzyaloshinskii–Moriya couplings in Majorana Cooper pair boxes

Manato Teranishi,<sup>1</sup> Shintaro Hoshino,<sup>2</sup> and Ai Yamakage<sup>1</sup>

<sup>1</sup>*Department of Physics, Nagoya University, Nagoya 464-8602, Japan*

<sup>2</sup>*Department of Physics, Chiba University, Chiba 263-8522, Japan*

(Dated: March 4, 2026)

We theoretically study how to design spin couplings in networks of Majorana Cooper pair boxes (MCBs) connected by multiple normal-metal leads. The inter-box interaction is generated by the conduction-electron-mediated Ruderman–Kittel–Kasuya–Yosida (RKKY) interaction. We show that the connectivity of Majoranas to the leads enables arbitrary types of couplings. As concrete examples, we show the realization of the XY exchange interaction and the Dzyaloshinskii–Moriya (DM) interaction, which are difficult to implement in previously proposed MCB-based schemes. The sign and magnitude of the couplings can be tuned continuously via gate-controlled tunneling amplitudes. These results establish MCBs as a versatile platform for engineered quantum spin systems.

## I. INTRODUCTION

Quantum spin systems serve as a fundamental platform for understanding diverse quantum phenomena, such as magnetism and topological phases. Recent advances in quantum simulation techniques have enabled the realization of various quantum spin models using ultracold atomic systems, such as the Ising model [1–12], the XY model [13–15], the XXZ model [16–19], and the XYZ model [20, 21]. Moreover, theoretical studies propose the realizations of Dzyaloshinskii–Moriya (DM) interactions [22–26], spin-1 models [27, 28], and the Kitaev model [29, 30].

Parallel to these developments, Majorana Cooper pair boxes (MCBs), mesoscopic superconducting islands hosting Majoranas, have emerged as a promising alternative platform for realizing quantum spin systems [31–37]. A MCB comprises multiple topological superconducting nanowires with localized Majoranas at their ends [38–40]. Due to the large charging energy, an effective spin-1/2 degree of freedom is defined on a MCB [41, 42]. Therefore, constructing a network of MCBs is a central strategy for designing quantum spin systems with MCBs. This scheme realizes a wide variety of spin models, including the XYZ model and the transverse-field Ising model [32]. Furthermore, it has been suggested that a two-dimensional arrangement of MCBs can lead to the realization of the Kitaev model, offering a platform for quantum spin liquids [31, 32, 36]. Intriguingly, proposals for exotic systems such as the spin-1 Blume–Capel model with supersymmetry [33], models exhibiting fracton phases [34], and non-Hermitian models hosting Yang–Lee anyons [37], highlight the versatility of MCBs as a platform for engineering unconventional quantum spin systems.

However, existing protocols for MCB-based quantum spin systems have not yet established methods for generating arbitrary spin–spin couplings. Specifically, designs for XY-type interactions and asymmetric spin interactions, such as the DM interaction, remain unexplored. In this work, we address this challenge by

utilizing the Ruderman–Kittel–Kasuya–Yosida (RKKY) framework [36, 43–45] with various connection patterns of the leads. We elucidate that the freedom in the wiring pattern is the key to engineering diverse spin Hamiltonians and demonstrate the realizations of the XY interaction and the Heisenberg interaction with DM interactions.

This paper is organized as follows. In Sec. II, we introduce a general model consisting of two MCBs connected via normal metal leads and derive its low-energy effective Hamiltonian. In Sec. III, we derive the general form of the RKKY interaction mediating the coupling between the effective spins. We then demonstrate the engineering of specific spin couplings, including the XY coupling and the Heisenberg coupling with DM interactions, in Secs. III A and III B, respectively. In Sec. IV, we calculate the spin susceptibility of the leads for two cases: infinite-length leads and finite-length leads. In Sec. IV C, we estimate the energy scale of the RKKY interaction using realistic experimental parameters. Finally, Sec. V is devoted to the summary and discussion of future perspectives.

## II. MODEL

We consider two MCBs connected by multiple leads, as illustrated in Fig. 1. Each MCB consists of two semi-conducting nanowires with Rashba spin–orbit coupling placed on an *s*-wave superconductor, under a magnetic field. The nanowires are assumed to be in the topological superconducting phase hosting Majorana zero modes at the ends, and the corresponding Majorana operators are denoted by  $\gamma_i^\alpha$  ( $i = 1, 2, 3, 4$ ), where the superscript  $\alpha = L, R$  indicates the MCB at the left or right side, respectively. The mesoscopic size of the MCBs induces a large charging energy, which restricts the system to a fixed-parity sector, allowing each MCB to be treated as an effective spin-1/2 system. In this section, we describe the Hamiltonian of the system and then derive the effective Hamiltonian.

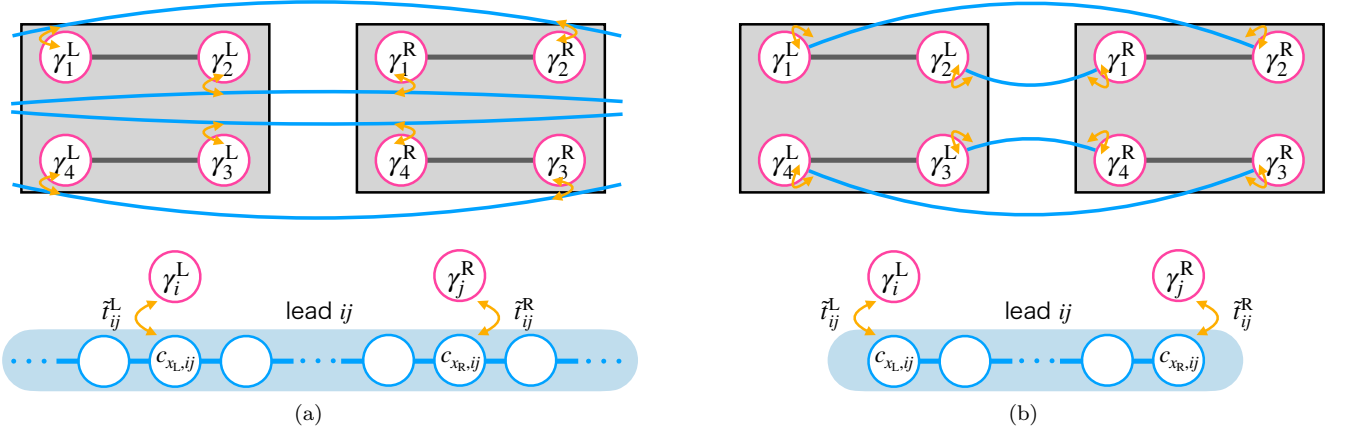


FIG. 1. Schematic setup for the two-spin system formed by two MCBs. The left (L) and right (R) boxes are MCBs with charging energy  $E_c^\alpha$  ( $\alpha = L, R$ ), where each of the four Majoranas (pink circles) is connected to leads (blue wires). Yellow double-headed arrows denote the tunnel coupling between the Majoranas and the leads. Panels (a) and (b) show the cases of infinite and finite leads, respectively.

### A. Two-box model

We consider a setup in which two MCBs, labeled L and R, are connected via multiple leads. We assume that each of the four Majoranas in one MCB is connected to all four Majoranas in the other, resulting in a total of 16 leads. The Hamiltonian  $\mathcal{H}$  is composed of the kinetic energy of the leads  $\mathcal{H}_{\text{lead}}$ , tunneling between leads and Majoranas  $\mathcal{H}_{\text{tun}}$ , charging energy of MCB  $\mathcal{H}_c$ , and hybridization of Majoranas  $\mathcal{H}_Z$ ,

$$\mathcal{H} = \mathcal{H}_{\text{lead}} + \mathcal{H}_{\text{tun}} + \mathcal{H}_c + \mathcal{H}_Z. \quad (1)$$

The first term is the lead Hamiltonian as a one-dimensional tight-binding model as follows:

$$\mathcal{H}_{\text{lead}} = \sum_{i,j=1}^4 \sum_r \left[ \varepsilon_0 c_{r,ij}^\dagger c_{r,ij} - t \left( c_{r,ij}^\dagger c_{r+1,ij} + \text{h.c.} \right) \right], \quad (2)$$

where  $\varepsilon_0$  is the on-site energy,  $t$  is the nearest-neighbor hopping energy, and  $c_{r,ij}^\dagger$  and  $c_{r,ij}$  denote the spinless electron creation and annihilation operators at a site  $r$  in the lead labeled by  $ij$ , respectively. Note that only the relevant spin projection of electrons, which is regarded as a spinless fermion, coupled to the Majoranas, is taken into account [46, 47]. We consider two types of lead configurations: infinite-length leads with periodic boundary conditions (PBC), as shown in Fig. 1(a), and finite-length leads with open boundary conditions (OBC), as shown in Fig. 1(b).

The second term  $\mathcal{H}_{\text{tun}}$ , which is the hybridization between the Majoranas and the electrons in the leads, is given by the following tunneling Hamiltonian [41, 48]

$$\mathcal{H}_{\text{tun}} = \sum_{i,j=1}^4 \left( \tilde{t}_{ij}^L \gamma_i^L c_{x_L,ij} + \tilde{t}_{ij}^R \gamma_j^R c_{x_R,ij} \right) + \text{h.c.}, \quad (3)$$

where  $\tilde{t}_{ij}^\alpha = t_{ij}^\alpha e^{i\phi_{\alpha,ij}}$  ( $t_{ij}^\alpha > 0$ ) denotes the tunneling amplitude between  $\gamma_i^\alpha$  and  $c_{x_\alpha,ij}$  ( $c_{x_\alpha,ij}^\dagger$ ) in the lead  $ij$  that connects  $\gamma_i^L$  and  $\gamma_j^R$ , and  $\phi_{\alpha,ij}$  is the relative phase difference between the phase of the superconducting order parameter of each MCB and each lead. As shown in the bottom panel of Fig. 1, the electron is hybridized with the Majoranas at  $x_L$  on the left MCB and  $x_R$  on the right MCB, respectively. Here, the  $i$ th Majorana operator in the MCB labeled  $\alpha$  satisfies

$$\gamma_i^\alpha = \gamma_i^{\alpha\dagger}, \quad \{ \gamma_i^\alpha, \gamma_j^\beta \} = 2\delta_{ij}\delta_{\alpha\beta}. \quad (4)$$

The third term  $\mathcal{H}_c$  denotes the charging energies of the MCBs and is given by

$$\mathcal{H}_c = \sum_{\alpha=L,R} E_c^\alpha (\mathcal{N}^\alpha - N_g^\alpha)^2, \quad (5)$$

where  $E_c^\alpha$  is the charging energy of each MCB,  $\mathcal{N}^\alpha$  is the total electron number operator in each MCB, and  $N_g^\alpha$  is the gate charge, which is tuned externally by applying a backgate voltage.

The last term  $\mathcal{H}_Z$  describes the overlap of Majorana wavefunctions, and is written as follows [49]:

$$\mathcal{H}_Z = i \sum_{\alpha=L,R} \sum_{i,j=1}^4 \tau_{ij}^\alpha \gamma_i^\alpha \gamma_j^\alpha, \quad (6)$$

where the coupling constant is antisymmetric as  $\tau_{ij}^\alpha = -\tau_{ji}^\alpha$ . The subscript “Z” derives from the fact that it gives rise to a Zeeman term in the effective spin system. The magnitude and sign of this term can be controlled by tuning the nanowire length and chemical potential.

## B. Mapping from Majoranas to spin degrees of freedom

In this paper, we focus on the case where the charging energy is the largest energy scale in the system, and the fermion parity for each MCB is fixed as [32]

$$\mathcal{P}^\alpha = (i\gamma_1^\alpha \gamma_2^\alpha)(i\gamma_3^\alpha \gamma_4^\alpha) = \pm 1. \quad (7)$$

As a result, the degrees of freedom of the fixed-parity subspace are reduced from  $2^2 = 4$  to 2, which is represented as a spin-1/2

$$S_i^\alpha := \frac{1}{2} \sum_{j,k=1}^3 \varepsilon_{ijk} L_{jk}^\alpha = \mathcal{P}^\alpha L_{i4}^\alpha, \quad (8)$$

where  $\varepsilon_{ijk}$  is the Levi-Civita symbol, and  $L_{jk}^\alpha := -i\gamma_j^\alpha \gamma_k^\alpha / 2$ . The spin operators  $S_1$ ,  $S_2$ , and  $S_3$  correspond to  $S_x$ ,  $S_y$ , and  $S_z$ , respectively.

## C. Effective Hamiltonian

We consider the low-energy effective theory given by the Schrieffer-Wolff transformation [50] within the second-order perturbation of Eq. (3) when the tunneling amplitudes are sufficiently small compared to the charging energy ( $t_{ij}^\alpha / E_c^\alpha \ll 1$ ). The effective Hamiltonian is given by

$$\mathcal{H}_{\text{eff}} = \mathcal{H}_{\text{lead}} + \mathcal{H}' + \mathcal{H}_{\text{scatt}} + \mathcal{H}_Z, \quad (9)$$

with

$$\begin{aligned} \mathcal{H}' = 2 \sum_{i \neq j} \sum_{k,l=1}^4 & \left[ \frac{(\tilde{t}_{ik}^L)^* \tilde{t}_{jl}^L}{E_c^L} \gamma_j^L \gamma_i^L c_{x_L,ik}^\dagger c_{x_L,jl} \right. \\ & \left. + \frac{(\tilde{t}_{ki}^R)^* \tilde{t}_{lj}^R}{E_c^R} \gamma_j^R \gamma_i^R c_{x_R,ki}^\dagger c_{x_R,lj} \right], \quad (10) \end{aligned}$$

where the sum  $\sum_{i \neq j}$  runs from 1 to 4. The  $i = j$  term corresponds to a potential scattering  $\mathcal{H}_{\text{scatt}}$ . In the lowest-order perturbation calculation of the RKKY interaction in Sec. III, this term does not contribute spin degrees of freedom; therefore, it is neglected in this paper.

Next, we rewrite the effective Hamiltonian Eq. (9) in spin representation by Eq. (8) as

$$\mathcal{H}' = \sum_{i < j} \sum_{k,l} \left( T_{ik,jl}^L L_{ij}^L J_{ik,jl}^L + T_{ki,lj}^R L_{ij}^R J_{ki,lj}^R \right), \quad (11)$$

where  $T_{ij,kl}^\alpha := 4t_{ij}^\alpha t_{kl}^\alpha / E_c^\alpha$  is a coupling constant defined for a pair of leads  $ij$  and  $kl$ .  $J_{ij,kl}^\alpha$  is defined from the electron operators in the leads as

$$J_{ij,kl}^\alpha := -ie^{-i(\phi_{\alpha,ij} - \phi_{\alpha,kl})} c_{x_\alpha,ij}^\dagger c_{x_\alpha,kl} + \text{h.c.}, \quad (12)$$

which is interpreted as the generators of the SO(16) symmetry group corresponding to the conduction-electron spin operator.

The bilinear part of the Majorana operators is regarded as the Zeeman term

$$\mathcal{H}_Z = \sum_\alpha \sum_i B_i^\alpha S_i^\alpha, \quad (13)$$

where  $B_i^\alpha = -4(\tau_{jk}^\alpha + \mathcal{P}^\alpha \tau_{i4}^\alpha)$ .

## III. RKKY INTERACTION

In the weak coupling regime where  $T_{ij,kl}^\alpha$  is small, an effective exchange interaction, the RKKY interaction, emerges between localized spins formed by Majoranas, mediated by conduction electrons in the leads. First, we derive the RKKY interaction  $\mathcal{H}_{\text{RKKY}} = \sum_{i < j} \sum_{i' < j'} \mathcal{J}_{ij,i'j'} L_{ij}^L L_{i'j'}^R$  for our model. The RKKY interaction can be obtained from the second-order correction to the free energy as follows [51, 52]:

$$\begin{aligned} \mathcal{J}_{ij,i'j'} = -T \sum_{klk'l'} & T_{ik,jl}^L T_{k'i',l'j'}^R \int_0^{1/T} d\tau_1 \int_0^{1/T} d\tau_2 \\ & \times \langle T_\tau J_{ik,jl}^L(\tau_1) J_{k'i',l'j'}^R(\tau_2) \rangle, \quad (14) \end{aligned}$$

where the average  $\langle \dots \rangle = \text{tr}(e^{-\mathcal{H}_{\text{lead}}/T} \dots) / \text{tr}(e^{-\mathcal{H}_{\text{lead}}/T})$  is taken for the connected terms. By performing the integration over imaginary time, we obtain the following result (see Appendix A for details),

$$\mathcal{J}_{ij,i'j'} = \mathcal{T}_{ij'} \mathcal{T}_{j'i'} \tilde{\chi}_{ij',j'i'} - \mathcal{T}_{i'i'} \mathcal{T}_{j'j'} \tilde{\chi}_{i'i',j'j'}, \quad (15)$$

where we define the product of the tunneling amplitudes between Majoranas in lead  $ij$  as  $\mathcal{T}_{ij} := 4t_{ij}^L t_{ij}^R / \sqrt{E_c^L E_c^R}$ . Moreover,

$$\tilde{\chi}_{ij,kl} := 2\text{Re} \left[ e^{i(\Delta\phi_{ij} - \Delta\phi_{kl})} \chi_{ij,kl} \right], \quad (16)$$

where

$$\begin{aligned} \chi_{ij,kl} = -T \int_0^{1/T} d\tau_1 \int_0^{1/T} d\tau_2 \\ \times \left\langle T_\tau c_{x_n,ij}(\tau_1) c_{x_m,ij}^\dagger(\tau_2) c_{x_m,kl}(\tau_2) c_{x_n,kl}^\dagger(\tau_1) \right\rangle, \quad (17) \end{aligned}$$

corresponds to the static spin susceptibility defined by the two leads  $ij$  and  $kl$ , and  $\Delta\phi_{ij} := \phi_{L,ij} - \phi_{R,ij}$ .

Finally, by rewriting  $\mathcal{H}_{\text{RKKY}}$  from the operator  $L_{ij}^\alpha$  to the spin operator  $S_i^\alpha$  using Eq. (8), we obtain the RKKY Hamiltonian between the spins at the left and right MCBs,

$$\mathcal{H}_{\text{RKKY}} = \sum_{i,i'} \mathcal{J}_{ii'} S_i^L S_{i'}^R. \quad (18)$$

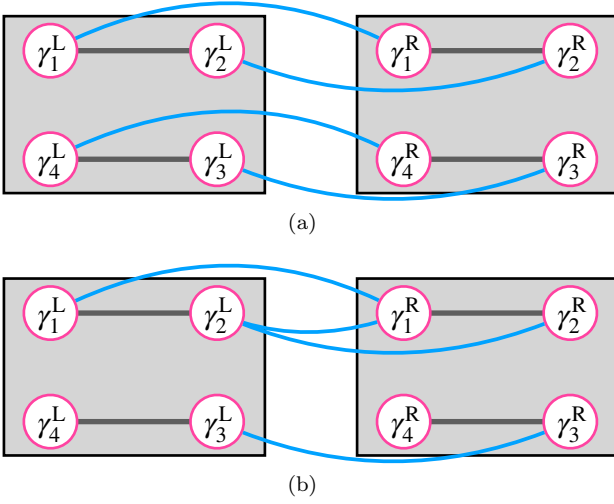


FIG. 2. Schematic setups for realizing (a) the XY coupling and (b) the Heisenberg + DM coupling.

Exploiting the antisymmetry of the original coupling constant,  $\mathcal{J}_{jk,j'k'} = -\mathcal{J}_{kj,j'k'} = -\mathcal{J}_{jk,k'j'}$ , the resultant coupling constant  $\mathcal{J}_{ii'}$  is explicitly expressed as follows:

$$\begin{aligned} \mathcal{J}_{ii'} &= \frac{1}{4} \varepsilon_{ijk} \varepsilon_{i'j'k'} \mathcal{J}_{jk,j'k'} + \frac{1}{2} \varepsilon_{i'j'k'} \mathcal{P}^L \mathcal{J}_{i4,j'k'} \\ &+ \frac{1}{2} \varepsilon_{ijk} \mathcal{P}^R \mathcal{J}_{jk,i'4} + \mathcal{P}^L \mathcal{P}^R \mathcal{J}_{i4,i'4}, \end{aligned} \quad (19)$$

where summation over repeated indices ( $j, k, j', k' \in \{1, 2, 3\}$ ) is implied.

The coupling constant Eq. (19) can be controlled by tuning the tunneling amplitude via gate voltages, the susceptibility of the leads by adjusting their lengths or chemical potentials, and the phase difference between the superconducting order parameters by driving a Josephson current.

In the following, we apply the theory to the XY and the Heisenberg + DM couplings. We provide a specific wiring configuration and treat the tunneling amplitudes as the only externally modulated parameters.

### A. XY coupling

We consider the XY-type spin coupling given by

$$\mathcal{H} = J \sum_{\mu=x,y} S_{\mu}^L S_{\mu}^R, \quad (20)$$

utilizing a configuration with four leads,  $ij = 11, 22, 33,$  and  $44$ , as illustrated in Fig. 2(a). In this case,  $\mathcal{T}_{ij} = 0$  for  $i \neq j$ , and the diagonal components of the coupling constants in Eq. (19) satisfy  $\mathcal{J}_{ii} = -\sum_{j < k} |\varepsilon_{ijk}| \mathcal{T}_{jj} \mathcal{T}_{kk} \tilde{\chi}_{jj,kk} - \mathcal{P}^L \mathcal{P}^R \mathcal{T}_{ii} \mathcal{T}_{44} \tilde{\chi}_{ii,44}$ . We now examine how the RKKY interaction  $\mathcal{J}$  can be controlled via  $\mathcal{T}$ . Imposing the condition  $\mathcal{J}_{zz} = 0$  for the XY cou-

pling yields

$$\tilde{\mathcal{T}}_{33} = -\mathcal{P}^L \mathcal{P}^R \frac{\tilde{\chi}_{11,22}}{\tilde{\chi}_{33,44}} \tilde{\mathcal{T}}_{11} \tilde{\mathcal{T}}_{22}, \quad (21)$$

where  $\tilde{\mathcal{T}}_{ii} := \mathcal{T}_{ii}/\mathcal{T}_{44}$  ( $i = 1, 2, 3$ ) are normalized parameters that can be tuned externally. Since the product of the tunneling amplitudes  $\mathcal{T}_{ii}$  is always a positive real number, the product of the fermion parities and the spin susceptibilities must satisfy the sign condition:  $\text{sgn}(\mathcal{P}^L \mathcal{P}^R \tilde{\chi}_{11,22}/\tilde{\chi}_{33,44}) = -1$ . If +1 is chosen, it means there exists no  $\mathcal{T}_{33}$  satisfying  $\mathcal{J}_{zz} = 0$ . Substituting this into the expressions for  $\mathcal{J}_{xx}$  and  $\mathcal{J}_{yy}$ , we obtain

$$\tilde{\mathcal{J}}_{xx} = \tilde{\mathcal{T}}_{11} \tilde{\mathcal{T}}_{22}^2 - \tilde{B}_x \tilde{\mathcal{T}}_{11}, \quad (22)$$

$$\tilde{\mathcal{J}}_{yy} = \tilde{A}_y \tilde{\mathcal{T}}_{11}^2 \tilde{\mathcal{T}}_{22} - \tilde{B}_y \tilde{\mathcal{T}}_{22}, \quad (23)$$

where  $\tilde{\mathcal{J}}_{ii} := \mathcal{J}_{ii}/(A_x \mathcal{T}_{44}^2)$  are the dimensionless coupling constants, and we introduce the normalized parameters  $\tilde{A}_y := A_y/A_x$  and  $\tilde{B}_i := B_i/A_x$ . The parameters  $A_i$  and  $B_i$  are defined as

$$A_i := \mathcal{P}^L \mathcal{P}^R \sum_{j < k} |\varepsilon_{ijk}| \frac{\tilde{\chi}_{11,22} \tilde{\chi}_{jj,kk}}{\tilde{\chi}_{33,44}}, \quad B_i := \mathcal{P}^L \mathcal{P}^R \tilde{\chi}_{ii,44}, \quad (24)$$

where the index  $i \in \{1, 2, 3\}$  corresponds to  $\{x, y, z\}$  on the left-hand sides. These parameters depend only on the fermion parities of each MCB and the susceptibilities of the leads. They are, therefore, intrinsic to the system and are treated as constants in this section.

Solving the isotropic condition with  $J = \mathcal{J}_{xx} = \mathcal{J}_{yy}$ , we obtain  $\tilde{\mathcal{T}}_{ii}$  as a function of the normalized coupling constant  $\tilde{J} := J/(A_x \mathcal{T}_{44}^2)$ . Although the general solution is complicated (see Appendix B), imposing the simplified conditions  $\tilde{B}_x = \tilde{A}_y \tilde{B}_y$  and  $\tilde{A}_y, \tilde{B}_y < 0$  reduces the problem to a quadratic equation, yielding simple analytical solutions:

$$\tilde{\mathcal{T}}_{11} = \sqrt{\left(\frac{\tilde{J}}{2\tilde{A}_y \tilde{B}_y}\right)^2 + \frac{\tilde{B}_y}{\tilde{A}_y}} - \frac{\tilde{J}}{2\tilde{A}_y \tilde{B}_y}, \quad (25)$$

$$\tilde{\mathcal{T}}_{22} = \sqrt{\left(\frac{\tilde{J}}{2\tilde{B}_y}\right)^2 + \tilde{A}_y \tilde{B}_y} - \frac{\tilde{J}}{2\tilde{B}_y}. \quad (26)$$

Figure 3 shows the solutions  $\tilde{\mathcal{T}}_{11}$  (solid blue line) and  $\tilde{\mathcal{T}}_{22}$  (dashed red line) as a function of the target coupling constant  $\tilde{J}$ . Since the parameters  $A_i$  and  $B_i$  are expected to be of the same order of magnitude, we set  $(\tilde{B}_x, \tilde{A}_y, \tilde{B}_y) = (1, -1, -1)$  for example. The plot shows that the sign of the interaction can be continuously tuned between ferromagnetic and antiferromagnetic regimes simply by adjusting the tunneling amplitudes.

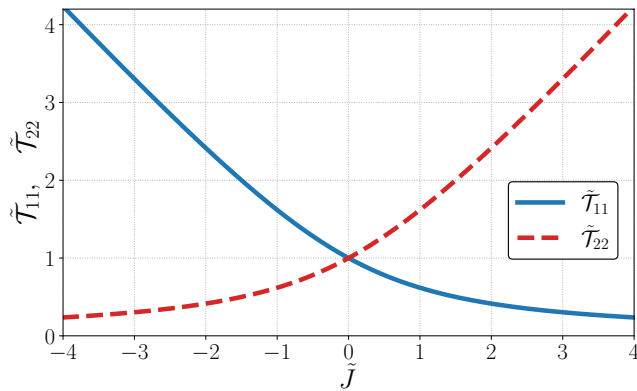


FIG. 3. Tunneling amplitudes realizing the XY coupling.  $\tilde{\mathcal{T}}_{11}$  (solid line) and  $\tilde{\mathcal{T}}_{22}$  (dotted line) as a function of  $J$  obtained from Eqs. (25) and (26), for  $(\tilde{B}_x, \tilde{A}_y, \tilde{B}_y) = (1, -1, -1)$ .

### B. Heisenberg + DM coupling

Next, we consider the case where both the Heisenberg and DM interactions are present, given by

$$\mathcal{H} = J \sum_{\mu=x,y,z} S_{\mu}^L S_{\mu}^R + D(S_x^L S_y^R - S_y^L S_x^R). \quad (27)$$

We focus on the configuration shown in Fig. 2(b), where only the leads  $ij = 11, 22, 33, 12,$  and  $21$  are connected. In this case, Eq. (19) implies that only  $\mathcal{J}_{\mu\mu}$ ,  $\mathcal{J}_{xy}$ , and  $\mathcal{J}_{yx}$  have finite values, while all other coupling constants are zero. By imposing the target conditions  $\mathcal{J}_{\mu\mu} = J$  and  $\mathcal{J}_{xy} = -\mathcal{J}_{yx} = D$ , we derive the required parameters for the Heisenberg + DM coupling (see Appendix C):

$$\mathcal{T}_{11} = -\frac{J}{\tilde{\chi}_{11,33}\tilde{\mathcal{T}}_{33}}, \quad \mathcal{T}_{22} = -\frac{J}{\tilde{\chi}_{22,33}\tilde{\mathcal{T}}_{33}}, \quad (28)$$

$$\mathcal{T}_{12} = -\frac{D}{\tilde{\chi}_{12,33}\tilde{\mathcal{T}}_{33}}, \quad \mathcal{T}_{21} = \frac{D}{\tilde{\chi}_{21,33}\tilde{\mathcal{T}}_{33}}, \quad (29)$$

$$\mathcal{T}_{33} = \sqrt{\frac{BD^2 - AJ^2}{J}}, \quad (30)$$

where  $A$  and  $B$  are defined as

$$A := \frac{\tilde{\chi}_{11,22}}{|\tilde{\chi}_{11,33}\tilde{\chi}_{22,33}|}, \quad B := \frac{\tilde{\chi}_{12,21}}{|\tilde{\chi}_{12,33}\tilde{\chi}_{21,33}|}. \quad (31)$$

Similar to the parameters discussed in Sec. III A, these are determined solely by the properties of the leads and are treated as constants in this section. Since  $\mathcal{T}_{33}$  is a positive real number,  $(BD^2 - AJ^2)/J > 0$ . The specific conditions for the existence of real solutions, categorized by the signs of  $A$  and  $B$ , are summarized in Table I. Furthermore, we visualize the regions satisfying these conditions in Fig. 4 by introducing the dimensionless parameters  $J/A$  and  $D/A$ . In these plots, we assume  $|B/A| = 1$  as a representative example. Note that cases (iii) and (iv) in Table I are equivalent to cases (ii) and (i), respectively,

TABLE I. The conditions for the existence of a real solution  $\mathcal{T}_{33}$  in Eq. (30).

conditions	$J > 0$	$J < 0$
(i) $A > 0, B > 0$	$ D  > \sqrt{\frac{A}{B}}J$	$ D  < \sqrt{\frac{A}{B}} J $
(ii) $A > 0, B < 0$	not exist	arbitrary $D$
(iii) $A < 0, B > 0$	arbitrary $D$	not exist
(iv) $A < 0, B < 0$	$ D  < \sqrt{\frac{A}{B}}J$	$ D  > \sqrt{\frac{A}{B}} J $

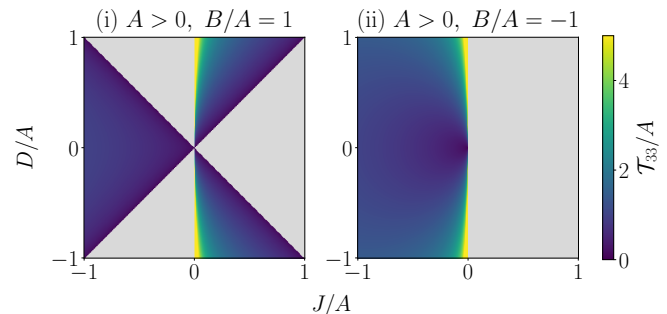


FIG. 4. Color maps representing the region in which a real solution  $\mathcal{T}_{33}$  exists in Eq. (30). The color bar indicates the value of  $\mathcal{T}_{33}/A$ .

under the sign reversal of the axes; therefore, we only plot the results for cases (i) and (ii) in Fig. 4. The colored regions in the figure represent the parameter space where the target Hamiltonian in Eq. (27) is realizable. The color gradient indicates the required value of the controllable parameter  $\mathcal{T}_{33}/A$  to achieve the specific desired values of  $(J, D)$ . As seen from Eq. (30), a small value of  $J$  is achieved by choosing a large value of  $\mathcal{T}_{33}$ . Furthermore, the slope of the boundary in case (i) is determined by the constant ratio  $A/B$ . In contrast, the gray regions signify the regimes where the target Hamiltonian cannot be realized, regardless of how  $\mathcal{T}_{33}$  is adjusted, as no real solution exists.

## IV. SPIN SUSCEPTIBILITY

In Secs. III A and III B, we focused on modulating the tunneling amplitudes while treating the susceptibilities of the leads as constants. In this section, we calculate the static spin susceptibility of the leads, defined in Eq. (17), using the tight-binding model given by Eq. (2) for two cases: infinite-length leads and finite-length leads. Based on these results, we finally estimate the magnitude of the RKKY interaction in Sec. IV C.

### A. Infinite-length leads

First, we consider infinite-length leads as shown in Fig. 1(a), where the crystal momentum  $k$  is a good quan-

tum number. The energy eigenvalues and eigenstates in Eq. (2) for each lead are given by

$$E_k = \varepsilon_0 - 2t \cos(ka), \quad (32)$$

$$|\psi_{k,ij}\rangle = \sum_{r=1}^{N_0} \phi_k(r) c_{r,ij}^\dagger |0\rangle, \quad (33)$$

$$\phi_k(r) = \frac{1}{\sqrt{N_0}} \exp(ikra), \quad (34)$$

where  $k$  is restricted to the first Brillouin zone  $-\pi/a \leq k \leq \pi/a$  and  $a$  is the lattice constant.  $N_0$  is the number of sites in the lead, which is taken to be sufficiently large ( $N_0 \rightarrow \infty$ ). Hereafter, we set the on-site energy  $\varepsilon_0$  to zero. The coupling sites are located at  $x_L = 1$  and  $x_R = N$  for all leads. To obtain an order-of-magnitude estimate of the coupling constant, we assume, for simplicity, that all leads are identical, and then the spin susceptibility in Eq. (17) reduces to the isotropic form [53], i.e., not dependent on  $ijkl$ .

$$\chi = -\left(\frac{a}{2\pi}\right)^2 \int_{-\frac{\pi}{a}}^{\frac{\pi}{a}} dk \int_{-\frac{\pi}{a}}^{\frac{\pi}{a}} dk' \frac{n_F(E_k) - n_F(E_{k'})}{E_k - E_{k'}} \times \cos[(k - k')(N - 1)a], \quad (35)$$

where  $n_F(E) = \theta(\varepsilon_F - E)$  is the Fermi-Dirac distribution function at zero temperature, and  $\varepsilon_F$  is the Fermi energy.

Figure 5 displays the calculated isotropic spin susceptibility  $\chi$  as a function of the distance  $N$  between the two spins  $\mathbf{S}^L$  and  $\mathbf{S}^R$ . The (black) square, (red) circle, and (blue) triangle symbols denote those for the Fermi energies  $\varepsilon_F/t = 0$ , located at the center of the energy band,  $-1$ , and  $-1.8$ , located near the bottom of the energy band, respectively. In all cases, the susceptibility exhibits oscillatory decay. As  $\varepsilon_F/t$  increases from the band bottom, the oscillation period, which corresponds to the Fermi wavelength, becomes shorter. Therefore, from the perspective of controllability, it is easier to control when the Fermi energy is low.

## B. Finite-length leads

Next, we consider finite-length leads as shown in Fig. 1(b) by imposing OBC on the leads Hamiltonian in Eq. (2):

$$\mathcal{H}_{\text{lead}}^{\text{OBC}} = \sum_{i,j=1}^4 \left[ \sum_{r=1}^N \varepsilon_0 c_{r,ij}^\dagger c_{r,ij} - t \sum_{r=1}^{N-1} \left( c_{r,ij}^\dagger c_{r+1,ij} + \text{h.c.} \right) \right], \quad (36)$$

where we assume  $x_L = 1$  and  $x_R = N$  similar to the infinite-length case. Then, the energy eigenvalues and

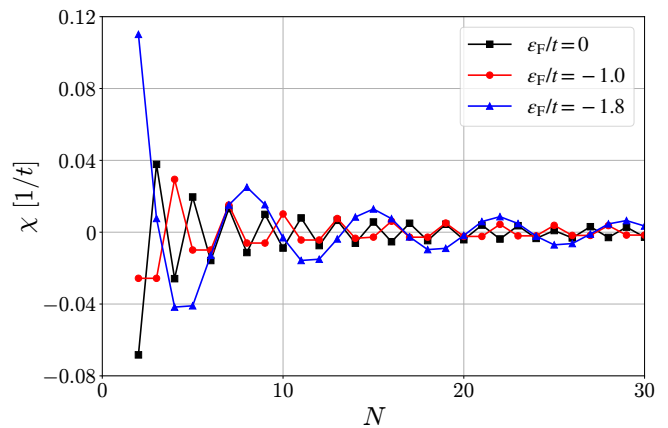


FIG. 5. Site  $N$  dependence of the isotropic spin susceptibility  $\chi$  for infinite length. The black, red, and blue lines correspond to the numerical calculation results of the susceptibility for Fermi energies of 0 (at the center of the energy band),  $-t$ , and  $-1.8t$  (around the bottom of the energy band), respectively.

eigenstates are given by

$$E_\lambda = \varepsilon_0 - 2t \cos\left(\frac{\lambda\pi}{N+1}\right) \quad (\lambda = 1, \dots, N), \quad (37)$$

$$|\psi_\lambda\rangle = \sum_{r=1}^N \phi_\lambda(r) c_{r,ij}^\dagger |0\rangle, \quad (38)$$

$$\phi_\lambda(r) = \frac{1}{\sqrt{\sum_{k=1}^N \sin^2\left(\frac{\lambda\pi k}{N+1}\right)}} \sin\left(\frac{\lambda\pi r}{N+1}\right), \quad (39)$$

where  $\lambda$  is the label of the eigenstate. This eigenfunction indeed satisfies the OBC  $\phi_\lambda(0) = \phi_\lambda(N+1) = 0$ .

The isotropic spin susceptibility  $\chi$  in the finite-length case is calculated analogously to Eq. (35), by replacing the integration over the wavenumber  $k$  with a summation over the discrete quantum number  $\lambda$ :

$$\chi = - \sum_{\lambda, \lambda'=1}^N \frac{n_F(E_\lambda) - n_F(E_{\lambda'})}{E_\lambda - E_{\lambda'}} \times \phi_\lambda(N) \phi_{\lambda'}^*(1) \phi_{\lambda'}(1) \phi_{\lambda'}^*(N). \quad (40)$$

Figure 6 shows the  $N$ -dependence of the spin susceptibility for the finite-length case. It decays approximately as  $1/N$  (see the inset). A significant difference from the infinite-length case is the absence of sign-changing oscillations. Consequently, from the perspective of controllability, this monotonic behavior is advantageous when one wishes to avoid unintended sign reversals.

## C. Order estimate of the RKKY interaction

In this section, we estimate the order of magnitude of the RKKY coupling constant in Eq. (18). We assume

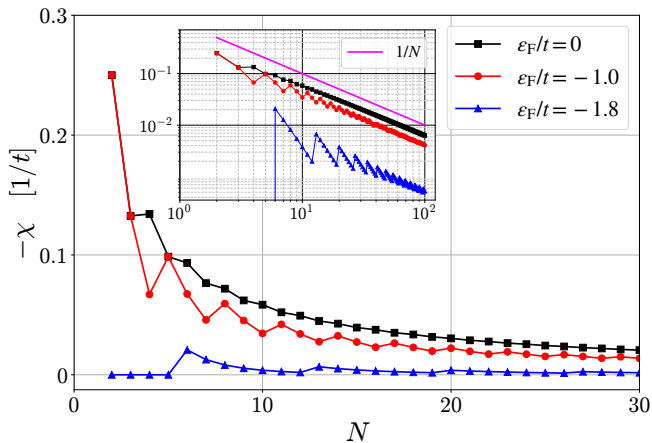


FIG. 6. The isotropic spin susceptibility for finite length cases at three different Fermi energies: 0,  $-t$ , and  $-1.8t$ . The inset is a double-logarithmic plot that shows the decay is approximately as  $1/N$ .

that the hopping energy  $t$  within the leads is of the order of 1 eV, and the Fermi energy is  $\varepsilon_F = -1.8t$ . For the finite-length leads, the magnitude of the isotropic spin susceptibility at a length  $l \sim 10$  nm ( $N = 30$ ,  $a = 3.3$  Å) between two MCBs is estimated to be at most  $|\chi| \sim 0.1$  /eV. The charging energy  $E_c$  of an MCB is on the order of 1 meV [54]. While the perturbative expansion requires  $t_{\text{tun}} \ll E_c$ , we nevertheless adopt a rather large value of  $t_{\text{tun}} = E_c/2$  within the acceptable range to evaluate the possible scale of the RKKY coupling. Here,  $t_{\text{tun}}$  denotes the typical magnitude of a tunneling amplitude  $\tilde{t}_{ij}$  between a Majorana and an electron in the lead. Accordingly, the magnitude of the uniform coupling  $\mathcal{T}_{ij}$  in Eq. (15) is estimated as  $\mathcal{T} \approx 4t_{\text{tun}}^2/E_c = 1$  meV. Finally, the strength of the RKKY interaction is estimated as  $|\mathcal{J}_{\text{RKKY}}| \approx \mathcal{T}^2|\chi| \sim 0.1$   $\mu\text{eV}$ . This energy scale corresponds to a temperature of approximately 1 mK, which is within the reach of current experimental techniques.

## V. SUMMARY

We have theoretically demonstrated that connecting MCBs via multiple normal metal leads provides a versatile framework for engineering spin couplings described by quadratic spin Hamiltonians. Our central finding is that the wiring patterns of the leads serve as a crucial degree of freedom for determining the form of the resulting RKKY interaction. Our method realizes not only the standard Heisenberg interaction but also the XY interaction and asymmetric terms such as the DM interaction,

which is tuned by modulating the tunneling amplitude via gate voltages, adjusting the length or chemical potential of the leads, and inducing a phase difference between the superconducting order parameters by driving a Josephson current.

The design established here for a two-MCB system can be extended to larger networks. By arranging MCBs in one- or two-dimensional lattices and engineering the wiring patterns accordingly, our approach provides a versatile platform for exploring a diverse range of quantum spin systems.

Finally, we comment on the validity of the perturbative approach used in this work. Our derivation of the RKKY interaction assumes a weak coupling regime between the Majoranas and the conduction electrons. However, in the strong coupling regime, it is known that MCB systems can exhibit the topological Kondo effect, characterized by non-Fermi liquid behavior [41, 55–61]. Consequently, a competition between the RKKY interaction and the topological Kondo effect is expected, analogous to the Doniach phase diagram in heavy fermion systems [62]. Exploring the phase diagram and the crossover between these regimes remains an intriguing and important task for future research.

## ACKNOWLEDGMENTS

M.T. was supported by JST SPRING (Grant No. JP-MJSP2125). S.H. was supported by JSPS KAKENHI (Grant Nos. 23K17668, 24K00578, and 24K00583) and the Grant-in-Aid for Transformative Research Areas (A) “Correlation Design Science” (Grant No. JP25H01249). A.Y. was supported by JSPS KAKENHI (Grant Nos. JP24H00853 and JP25K07224).

## Appendix A: RKKY coupling

Here, we derive the RKKY coupling Eq. (15). First, we define the Matsubara Green’s function as

$$\begin{aligned} G_{ab,cd}(x_L, x_R; \tau_1 - \tau_2) &= -\left\langle T_\tau c_{x_L,ab}(\tau_1) c_{x_R,cd}^\dagger(\tau_2) \right\rangle \\ &= G_{ab}(x_L, x_R; \tau_1 - \tau_2) \delta_{ac} \delta_{bd}. \end{aligned} \quad (\text{A1})$$

This Green’s function involves two leads,  $ab$  and  $cd$ , but because there is no interaction between different leads, it simplifies as shown in the second line. Using this Green’s function, Eq. (14) can be rewritten as follows:

$$\begin{aligned} \mathcal{J}_{ij,i'j'} &= T_{ij',j'i'}^L T_{ji',ij'}^R \left[ e^{i(\Delta\phi_{ij'} - \Delta\phi_{ji'})} \chi_{ij',j'i'} + e^{-i(\Delta\phi_{ij'} - \Delta\phi_{ji'})} \chi_{ji',ij'} \right] \\ &\quad - T_{ii',jj'}^L T_{ii',jj'}^R \left[ e^{i(\Delta\phi_{ii'} - \Delta\phi_{jj'})} \chi_{ii',jj'} + e^{-i(\Delta\phi_{ii'} - \Delta\phi_{jj'})} \chi_{jj',ii'} \right], \end{aligned} \quad (\text{A2})$$

where

$$\chi_{ab,cd} = -T \int_0^{1/T} d\tau_1 \int_0^{1/T} d\tau_2 G_{ab}(x_L, x_R; \tau_1 - \tau_2) G_{cd}(x_R, x_L; \tau_2 - \tau_1). \quad (\text{A3})$$

In addition, we perform a Fourier transform of the Matsubara Green's function into Matsubara frequency space

$$G_{ab}(x_L, x_R; \tau) = T \sum_l G_{ab}(x_L, x_R; i\omega_l) e^{-i\omega_l \tau}, \quad (\text{A4})$$

where  $\omega_l = (2l + 1)\pi T$  and  $l$  is an integer. Furthermore, by rewriting the Matsubara frequency summation as a contour integral in the complex plane, Eq. (A3) reduces to

$$\begin{aligned} \chi_{ab,cd} &= \int_{-\infty}^{\infty} \frac{d\varepsilon}{2\pi i} n_F(\varepsilon) \left[ G_{ab}^R(x_L, x_R; \varepsilon) G_{cd}^R(x_R, x_L; \varepsilon) \right. \\ &\quad \left. - G_{ab}^A(x_L, x_R; \varepsilon) G_{cd}^A(x_R, x_L; \varepsilon) \right], \end{aligned} \quad (\text{A5})$$

where  $n_F(\varepsilon) = (e^{\varepsilon/T} + 1)^{-1}$  is the Fermi-Dirac distribution function and the superscripts R/A denote the retarded/advanced Green's function. Using the relationship  $[G_{ab}^R(x_L, x_R; \varepsilon)]^* = G_{ab}^A(x_R, x_L; \varepsilon)$ , we obtain the relationship  $\chi_{ab,cd}^* = \chi_{cd,ab}$  from Eq. (A5). Applying this relationship to rewrite Eq. (A2), we obtain Eq. (15).

In particular, when the system has inversion symmetry, or when the lead index of the Green's function is irrelevant, Eq. (A5) simplifies and can be written as follows at zero temperature:

$$\chi_{ab,cd} = \frac{1}{\pi} \int_{-\infty}^{\varepsilon_F} d\varepsilon \text{Im} \left[ G_{ab}^R(x_L, x_R; \varepsilon) G_{cd}^R(x_R, x_L; \varepsilon) \right]. \quad (\text{A6})$$

## Appendix B: XY coupling

In Sec. III A, we consider only a particularly simple case. Here, we present the general conditions under which the XY coupling is realized. First, by eliminating  $\tilde{\mathcal{T}}_{22}$  from Eqs. (22) and (23), we obtain

$$\tilde{J} = \left[ \left( \frac{\tilde{J}}{\tilde{A}_y \tilde{\mathcal{T}}_{11}^2 - \tilde{B}_y} \right)^2 - \tilde{B}_x \right] \tilde{\mathcal{T}}_{11}. \quad (\text{B1})$$

Here, the following two conditions are imposed:  $\tilde{A}_y \tilde{\mathcal{T}}_{11}^2 - \tilde{B}_y \neq 0$ , and  $\text{sgn}(\tilde{J}) = \text{sgn}(\tilde{A}_y \tilde{\mathcal{T}}_{11}^2 - \tilde{B}_y)$ . The latter is

equivalent to  $\tilde{\mathcal{T}}_{22} > 0$ . Solving  $\tilde{J}$  as a function of  $\tilde{\mathcal{T}}_{11}$ , we obtain two solutions

$$\tilde{J}_{\pm} = \frac{(\tilde{A}_y \tilde{\mathcal{T}}_{11}^2 - \tilde{B}_y)^2}{2\tilde{\mathcal{T}}_{11}} \left( 1 \pm \sqrt{1 + \frac{4\tilde{B}_x \tilde{\mathcal{T}}_{11}^2}{(\tilde{A}_y \tilde{\mathcal{T}}_{11}^2 - \tilde{B}_y)^2}} \right), \quad (\text{B2})$$

where the subscript  $\pm$  represents the two branches for  $\tilde{J}$ . Note that for  $\tilde{J}_{\pm}$  to have real solutions, the expression inside the square root must be nonnegative. Then,  $\tilde{\mathcal{T}}_{22}$  is given for these two branches as

$$\tilde{\mathcal{T}}_{22,\pm} = \frac{\tilde{J}_{\pm}}{\tilde{A}_y \tilde{\mathcal{T}}_{11}^2 - \tilde{B}_y}, \quad (\text{B3})$$

respectively.

Figure B1 shows  $\tilde{\mathcal{T}}_{11}$  and  $\tilde{\mathcal{T}}_{22}$  as functions of  $\tilde{J}$ , obtained from Eqs. (B2) and (B3), respectively. Here, since the constants  $A_i$  and  $B_i$  are of the same order of magnitude, we set  $|\tilde{B}_x| = |\tilde{A}_y| = |\tilde{B}_y| = 1$ . The blue line represents  $\mathcal{T}_{11}$ , the red line represents  $\mathcal{T}_{22}$ , and the solid and dashed lines correspond to the  $\tilde{J}_{\pm}$  branches, respectively. The cases of  $(\tilde{B}_x, \tilde{A}_y, \tilde{B}_y) = (-1, 1, 1)$  and  $(-1, -1, 1)$  are not plotted because no real solutions exist, i.e., the XY coupling cannot be realized. Note that in case (a), the blue line and the red line are completely overlapping. In cases (e) and (f), there can be two possible values of  $\tilde{J}$  for a single value of  $\tilde{\mathcal{T}}_{11}$ . However, since  $\tilde{\mathcal{T}}_{22}$  also has two branches corresponding to the two branches of  $\tilde{J}_{\pm}$ , specifying the pair  $(\tilde{\mathcal{T}}_{11}, \tilde{\mathcal{T}}_{22})$  uniquely determines  $\tilde{J}$ . Among the six panels, the most convenient case is (d), where the value of  $\tilde{J}$  can be controlled relatively freely, including both positive and negative values, by modulating  $\tilde{\mathcal{T}}_{11}$  and  $\mathcal{T}_{22}$  with the gate voltage.

To summarize, first, from Eq. (B2), the value of variable  $\mathcal{T}_{11}$  is determined for the desired  $J$ . Next, from Eq. (B3), the value of variable  $\mathcal{T}_{22}$  is also uniquely determined. Finally, by determining the remaining value of  $\mathcal{T}_{33}$  from Eq. (21), we can realize the XY coupling with the desired coupling constant  $J$ .

## Appendix C: Heisenberg + DM coupling

Here, we derive the conditions for the realization of the Heisenberg + DM coupling. Now we consider the

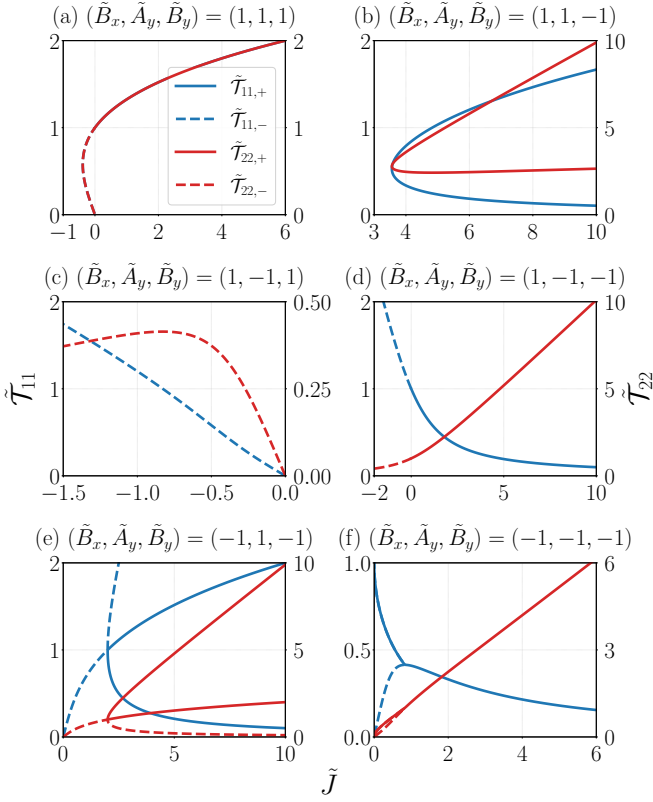


FIG. B1. Plots showing  $\tilde{\mathcal{T}}_{11}$  (left vertical axis, blue line) and  $\tilde{\mathcal{T}}_{22}$  (right vertical axis, red line) as functions of  $\tilde{J}$  for the case  $|\tilde{B}_x| = |\tilde{A}_y| = |\tilde{B}_y| = 1$ . The solid and dashed lines correspond to the  $\tilde{J}_+$  and  $\tilde{J}_-$  branches, respectively.

configuration shown in Fig. 2(b), where only the leads 11, 22, 33, 12, and 21 are connected. In this case, according to Eq. (19), the coupling constants satisfy

$$\mathcal{J}_{xx} = -\mathcal{T}_{22}\mathcal{T}_{33}\tilde{\chi}_{22,33}, \quad (\text{C1})$$

$$\mathcal{J}_{yy} = -\mathcal{T}_{11}\mathcal{T}_{33}\tilde{\chi}_{11,33}, \quad (\text{C2})$$

$$\mathcal{J}_{zz} = \mathcal{T}_{12}\mathcal{T}_{21}\tilde{\chi}_{12,21} - \mathcal{T}_{11}\mathcal{T}_{22}\tilde{\chi}_{11,22}, \quad (\text{C3})$$

$$\mathcal{J}_{xy} = \mathcal{T}_{21}\mathcal{T}_{33}\tilde{\chi}_{21,33}, \quad (\text{C4})$$

$$\mathcal{J}_{yx} = \mathcal{T}_{12}\mathcal{T}_{33}\tilde{\chi}_{12,33}, \quad (\text{C5})$$

and all other  $\mathcal{J}_{ij}$  are zero.

First, from the condition  $\mathcal{J}_{xx} = \mathcal{J}_{yy} = J$ , we obtain

$$-\tilde{\chi}_{22,33}\mathcal{T}_{22} = -\tilde{\chi}_{11,33}\mathcal{T}_{11} = \frac{J}{\mathcal{T}_{33}}. \quad (\text{C6})$$

Since  $\mathcal{T}_{ij} \geq 0$ , the following condition holds:  $\text{sgn}(J) = -\text{sgn}(\tilde{\chi}_{11,33}) = -\text{sgn}(\tilde{\chi}_{22,33})$ . It thus follows that  $\tilde{\chi}_{11,33}$  and  $\tilde{\chi}_{22,33}$  must always have the same sign.

Next, from the condition  $\mathcal{J}_{xy} = -\mathcal{J}_{yx} = D$ , we obtain

$$\tilde{\chi}_{21,33}\mathcal{T}_{21} = -\tilde{\chi}_{12,33}\mathcal{T}_{12} = \frac{D}{\mathcal{T}_{33}}. \quad (\text{C7})$$

Therefore, the following condition is imposed:  $\text{sgn}(D) = -\text{sgn}(\tilde{\chi}_{12,33}) = \text{sgn}(\tilde{\chi}_{21,33})$ . It thus follows that  $\tilde{\chi}_{12,33}$  and  $\tilde{\chi}_{21,33}$  must always have opposite signs.

Finally, by substituting Eqs. (C6) and (C7) into the condition  $\mathcal{J}_{zz} = J$ , we obtain the conditions for  $J$  and  $D$  to realize the Heisenberg + DM coupling as follows:

$$\begin{cases} AJ^2 + \mathcal{T}_{33}^2 J - BD^2 = 0, \\ \text{sgn}(J) = -\text{sgn}(\tilde{\chi}_{11,33}) = -\text{sgn}(\tilde{\chi}_{22,33}), \\ \text{sgn}(D) = -\text{sgn}(\tilde{\chi}_{12,33}) = \text{sgn}(\tilde{\chi}_{21,33}), \end{cases} \quad (\text{C8})$$

It then follows that the externally controllable parameter  $\mathcal{T}_{33}$  can be written as a function of the target parameters  $J$  and  $D$  as Eq. (30).

- 
- [1] H. Labuhn, D. Barredo, S. Ravets, S. De Léséleuc, T. Macrì, T. Lahaye, and A. Browaeys, Tunable two-dimensional arrays of single Rydberg atoms for realizing quantum Ising models, *Nature* **534**, 667 (2016).
- [2] J. Zeiher, J.-y. Choi, A. Rubio-Abadal, T. Pohl, R. Van Bijnen, I. Bloch, and C. Gross, Coherent many-body spin dynamics in a long-range interacting Ising chain, *Phys. Rev. X* **7**, 041063 (2017).
- [3] H. Bernien, S. Schwartz, A. Keesling, H. Levine, A. Omran, H. Pichler, S. Choi, A. S. Zibrov, M. Endres, M. Greiner, V. Vuletić, and M. D. Lukin, Probing many-body dynamics on a 51-atom quantum simulator, *Nature*

**551**, 579 (2017).

- [4] S. De Léséleuc, S. Weber, V. Lienhard, D. Barredo, H. P. Büchler, T. Lahaye, and A. Browaeys, Accurate mapping of multilevel Rydberg atoms on interacting spin-1/2 particles for the quantum simulation of Ising models, *Phys. Rev. Lett.* **120**, 113602 (2018).
- [5] V. Lienhard, S. de Léséleuc, D. Barredo, T. Lahaye, A. Browaeys, M. Schuler, L.-P. Henry, and A. M. Läuchli, Observing the Space- and Time-Dependent Growth of Correlations in Dynamically Tuned Synthetic Ising Models with Antiferromagnetic Interactions, *Phys. Rev. X* **8**, 021070 (2018).

- [6] E. Guardado-Sanchez, P. T. Brown, D. Mitra, T. Devakul, D. A. Huse, P. Schauf, and W. S. Bakr, Probing the Quench Dynamics of Antiferromagnetic Correlations in a 2D Quantum Ising Spin System, *Phys. Rev. X* **8**, 021069 (2018).
- [7] A. Keesling, A. Omran, H. Levine, H. Bernien, H. Pichler, S. Choi, R. Samajdar, S. Schwartz, P. Silvi, S. Sachdev, P. Zoller, M. Endres, M. Greiner, V. Vuletić, and M. D. Lukin, Quantum Kibble–Zurek mechanism and critical dynamics on a programmable Rydberg simulator, *Nature* **568**, 207 (2019).
- [8] G. Semeghini, H. Levine, A. Keesling, S. Ebadi, T. T. Wang, D. Bluvstein, R. Verresen, H. Pichler, M. Kalinowski, R. Samajdar, A. Omran, S. Sachdev, A. Vishwanath, M. Greiner, V. Vuletić, and M. D. Lukin, Probing topological spin liquids on a programmable quantum simulator, *Science* **374**, 1242 (2021).
- [9] S. Ebadi, T. T. Wang, H. Levine, A. Keesling, G. Semeghini, A. Omran, D. Bluvstein, R. Samajdar, H. Pichler, W. W. Ho, S. Choi, S. Sachdev, M. Greiner, V. Vuletić, and M. D. Lukin, Quantum phases of matter on a 256-atom programmable quantum simulator, *Nature* **595**, 227 (2021).
- [10] D. Bluvstein, A. Omran, H. Levine, A. Keesling, G. Semeghini, S. Ebadi, T. T. Wang, A. A. Michailidis, N. Maskara, W. W. Ho, S. Choi, M. Serbyn, M. Greiner, V. Vuletić, and M. D. Lukin, Controlling quantum many-body dynamics in driven Rydberg atom arrays, *Science* **371**, 1355 (2021).
- [11] P. Scholl, M. Schuler, H. J. Williams, A. A. Eberharter, D. Barredo, K.-N. Schymik, V. Lienhard, L.-P. Henry, T. C. Lang, T. Lahaye, A. M. Läuchli, and A. Browaeys, Quantum simulation of 2D antiferromagnets with hundreds of Rydberg atoms, *Nature* **595**, 233 (2021).
- [12] V. Bharti, S. Sugawa, M. Mizoguchi, M. Kunimi, Y. Zhang, S. de Léséleuc, T. Tomita, T. Franz, M. Weidemüller, and K. Ohmori, Picosecond-Scale Ultrafast Many-Body Dynamics in an Ultracold Rydberg-Excited Atomic Mott Insulator, *Phys. Rev. Lett.* **131**, 123201 (2023).
- [13] A. P. Orioli, A. Signoles, H. Wildhagen, G. Günter, J. Berges, S. Whitlock, and M. Weidemüller, Relaxation of an Isolated Dipolar-Interacting Rydberg Quantum Spin System, *Phys. Rev. Lett.* **120**, 063601 (2018).
- [14] S. De Léséleuc, V. Lienhard, P. Scholl, D. Barredo, S. Weber, N. Lang, H. P. Büchler, T. Lahaye, and A. Browaeys, Observation of a symmetry-protected topological phase of interacting bosons with Rydberg atoms, *Science* **365**, 775 (2019).
- [15] C. Chen, G. Bornet, M. Bintz, G. Emperauger, L. Leclerc, V. S. Liu, P. Scholl, D. Barredo, J. Hauschild, S. Chatterjee, M. Schuler, A. M. Läuchli, M. P. Zaletel, T. Lahaye, N. Y. Yao, and A. Browaeys, Continuous symmetry breaking in a two-dimensional Rydberg array, *Nature* **616**, 691–695 (2023).
- [16] A. Signoles, T. Franz, R. F. Alves, M. Gärttner, S. Whitlock, G. Zürn, and M. Weidemüller, Glassy dynamics in a disordered Heisenberg quantum spin system, *Phys. Rev. X* **11**, 011011 (2021).
- [17] P. Scholl, H. J. Williams, G. Bornet, F. Wallner, D. Barredo, L. Henriot, A. Signoles, C. Hainaut, T. Franz, S. Geier, A. Tebben, A. Salzinger, G. Zürn, T. Lahaye, M. Weidemüller, and A. Browaeys, Microwave Engineering of Programmable  $XXZ$  Hamiltonians in Arrays of Rydberg Atoms, *PRX Quantum* **3**, 020303 (2022).
- [18] T. Franz, S. Geier, C. Hainaut, A. Signoles, N. Thaicharoen, A. Tebben, A. Salzinger, A. Braemer, M. Gärttner, G. Zürn, G. Zürn, and M. Weidemüller, Absence of thermalization in an interacting system of thousands of quantum spins, *arXiv:2207.14216* (2022).
- [19] T. Franz, S. Geier, C. Hainaut, A. Braemer, N. Thaicharoen, M. Hornung, E. Braun, M. Gärttner, G. Zürn, and M. Weidemüller, Observation of anisotropy-independent magnetization dynamics in spatially disordered Heisenberg spin systems, *Phys. Rev. Res.* **6**, 033131 (2024).
- [20] S. Geier, N. Thaicharoen, C. Hainaut, T. Franz, A. Salzinger, A. Tebben, D. Grimshandl, G. Zürn, and M. Weidemüller, Floquet Hamiltonian engineering of an isolated many-body spin system, *Science* **374**, 1149 (2021).
- [21] L.-M. Steinert, P. Osterholz, R. Eberhard, L. Festa, N. Lorenz, Z. Chen, A. Trautmann, and C. Gross, Spatially Tunable Spin Interactions in Neutral Atom Arrays, *Phys. Rev. Lett.* **130**, 243001 (2023).
- [22] N. Nishad, A. Keselman, T. Lahaye, A. Browaeys, and S. Tsesses, Quantum simulation of generic spin-exchange models in Floquet-engineered Rydberg-atom arrays, *Phys. Rev. A* **108**, 053318 (2023).
- [23] F. Percivalle, D. Rossini, T. Haug, O. Morsch, and L. Amico, Controlled flow of excitations in a ring-shaped network of Rydberg atoms, *Phys. Rev. A* **108**, 023305 (2023).
- [24] E. Kuznetsova, S. Mistakidis, S. T. Rittenhouse, S. F. Yelin, and H. Sadeghpour, Engineering chiral spin interactions with Rydberg atoms, *arXiv:2309.08795* (2023).
- [25] M. Kunimi, T. Tomita, H. Katsura, and Y. Kato, Proposal for simulating quantum spin models with the Dzyaloshinskii-Moriya interaction using Rydberg atoms and the construction of asymptotic quantum many-body scar states, *Phys. Rev. A* **110**, 043312 (2024).
- [26] H. Kuji, M. Kunimi, and T. Nikuni, Proposal for realizing quantum-spin systems on a two-dimensional square lattice with Dzyaloshinskii-Moriya interaction by Floquet engineering using Rydberg atoms, *Phys. Rev. A* **112**, 022614 (2025).
- [27] V. S. Liu, M. Bintz, M. Block, R. Samajdar, J. Kemp, and N. Y. Yao, Supersolidity and Simplex Phases in Spin-1 Rydberg Atom Arrays, *arXiv:2407.17554* (2024).
- [28] J. Mögerle, K. Brechtelsbauer, A. T. Gea-Caballero, J. Prior, G. Emperauger, G. Bornet, C. Chen, T. Lahaye, A. Browaeys, and H. P. Büchler, Spin-1 Haldane phase in a chain of Rydberg atoms, *arXiv:2410.21424* (2024).
- [29] M. Kalinowski, N. Maskara, and M. D. Lukin, Non-Abelian Floquet Spin Liquids in a Digital Rydberg Simulator, *Phys. Rev. X* **13**, 031008 (2023).
- [30] Y.-H. Chen, B.-Z. Wang, T.-F. J. Poon, X.-C. Zhou, Z.-X. Liu, and X.-J. Liu, Realization and detection of Kitaev quantum spin liquid with Rydberg atoms, *arXiv:2310.12905* (2023).
- [31] A. Thomson and F. Pientka, Simulating spin systems with Majorana networks, *arXiv:1807.09291* (2018).
- [32] E. Sagi, H. Ebisu, Y. Tanaka, A. Stern, and Y. Oreg, Spin liquids from Majorana zero modes in a Cooper-pair box, *Phys. Rev. B* **99**, 075107 (2019).
- [33] H. Ebisu, E. Sagi, and Y. Oreg, Supersymmetry in the Insulating Phase of a Chain of Majorana Cooper Pair Boxes, *Phys. Rev. Lett.* **123**, 026401 (2019).

- [34] Y. You and F. von Oppen, Building fracton phases by Majorana manipulation, *Phys. Rev. Res.* **1**, 013011 (2019).
- [35] Y. Oreg and F. von Oppen, Majorana Zero Modes in Networks of Cooper-Pair Boxes: Topologically Ordered States and Topological Quantum Computation, *Annu. Rev. Condens. Matter Phys.* **11**, 397 (2020).
- [36] A. M. Tsvelik, Simulating Exotic Phases of Matter with Bond-Directed Interactions with Arrays of Majorana-Cooper Pair Boxes, *Phys. Rev. Lett.* **125**, 197202 (2020).
- [37] T. Sanno, M. G. Yamada, T. Mizushima, and S. Fujimoto, Engineering Yang-Lee anyons via Majorana bound states, *Phys. Rev. B* **106**, 174517 (2022).
- [38] J. D. Sau, R. M. Lutchyn, S. Tewari, and S. Das Sarma, Generic New Platform for Topological Quantum Computation Using Semiconductor Heterostructures, *Phys. Rev. Lett.* **104**, 040502 (2010).
- [39] J. Alicea, Majorana fermions in a tunable semiconductor device, *Phys. Rev. B* **81**, 125318 (2010).
- [40] Y. Oreg, G. Refael, and F. von Oppen, Helical Liquids and Majorana Bound States in Quantum Wires, *Phys. Rev. Lett.* **105**, 177002 (2010).
- [41] B. Béri and N. R. Cooper, Topological Kondo Effect with Majorana Fermions, *Phys. Rev. Lett.* **109**, 156803 (2012).
- [42] S. Plugge, A. Rasmussen, R. Egger, and K. Flensberg, Majorana box qubits, *New J. Phys.* **19**, 012001 (2017).
- [43] M. A. Ruderman and C. Kittel, Indirect Exchange Coupling of Nuclear Magnetic Moments by Conduction Electrons, *Phys. Rev.* **96**, 99 (1954).
- [44] T. Kasuya, A Theory of Metallic Ferro- and Antiferromagnetism on Zener's Model, *Progress of Theoretical Physics* **16**, 45 (1956).
- [45] K. Yosida, Magnetic Properties of Cu-Mn Alloys, *Phys. Rev.* **106**, 893 (1957).
- [46] C. J. Bolech and E. Demler, Observing Majorana bound States in  $p$ -Wave Superconductors Using Noise Measurements in Tunneling Experiments, *Phys. Rev. Lett.* **98**, 237002 (2007).
- [47] J. Ekström, P. Recher, and T. L. Schmidt, Transport properties of coupled Majorana bound states in the Coulomb blockade regime, *Phys. Rev. B* **101**, 195420 (2020).
- [48] L. Fu, Electron Teleportation via Majorana Bound States in a Mesoscopic Superconductor, *Phys. Rev. Lett.* **104**, 056402 (2010).
- [49] A. Y. Kitaev, Unpaired Majorana fermions in quantum wires, *Phys.-Usp.* **44**, 131 (2001).
- [50] J. R. Schrieffer and P. A. Wolff, Relation between the Anderson and Kondo Hamiltonians, *Phys. Rev.* **149**, 491 (1966).
- [51] E. Kogan, RKKY interaction in graphene, *Phys. Rev. B* **84**, 115119 (2011).
- [52] D. O. Oriekhov and V. P. Gusynin, RKKY interaction in a doped pseudospin-1 fermion system at finite temperature, *Phys. Rev. B* **101**, 235162 (2020).
- [53] M. Zare and E. Sadeghi, Exchange interaction of magnetic impurities in a biased bilayer phosphorene nanoribbon, *Phys. Rev. B* **98**, 205401 (2018).
- [54] S. M. Albrecht, A. P. Higginbotham, M. Madsen, F. Kuemmeth, T. S. Jespersen, J. Nygård, P. Krogstrup, and C. M. Marcus, Exponential protection of zero modes in Majorana islands, *Nature* **531**, 206 (2016).
- [55] B. Béri, Majorana-Klein Hybridization in Topological Superconductor Junctions, *Phys. Rev. Lett.* **110**, 216803 (2013).
- [56] A. Altland and R. Egger, Multiterminal Coulomb-Majorana Junction, *Phys. Rev. Lett.* **110**, 196401 (2013).
- [57] A. Altland, B. Béri, R. Egger, and A. M. Tsvelik, Bethe ansatz solution of the topological Kondo model, *J. Phys. A Math. Theor.* **47**, 265001 (2014).
- [58] A. Altland, B. Béri, R. Egger, and A. M. Tsvelik, Multichannel Kondo Impurity Dynamics in a Majorana Device, *Phys. Rev. Lett.* **113**, 076401 (2014).
- [59] F. Buccheri, H. Babujian, V. E. Korepin, P. Sodano, and A. Trombettoni, Thermodynamics of the Topological Kondo Model, *Nucl. Phys. B* **896**, 52 (2015).
- [60] L. Herviou, K. Le Hur, and C. Mora, Many-terminal Majorana Island: From Topological to Multichannel Kondo Model, *Phys. Rev. B* **94**, 235102 (2016).
- [61] G. Li, Y. Oreg, and J. I. Väyrynen, Multichannel Topological Kondo Effect, *Phys. Rev. Lett.* **130**, 066302 (2023).
- [62] S. Doniach, The Kondo lattice and weak antiferromagnetism, *Physica B+C* **91**, 231 (1977).